

DNA translocation through an array of kinked nanopores

Zhu Chen¹, Yingbing Jiang², Darren R. Dunphy¹, David P. Adams², Carter Hodges², Nanguo Liu¹, Nan Zhang³, George Xomeritakis¹, Xiaozhong Jin⁴, N. R. Aluru⁴, Steven J. Gaik⁵, Hugh W. Hillhouse⁵ and C. Jeffrey Brinker^{1,2,6}*

Synthetic solid-state nanopores are being intensively investigated as single-molecule sensors for detection and characterization of DNA, RNA and proteins. This field has been inspired by the exquisite selectivity and flux demonstrated by natural biological channels and the dream of emulating these behaviours in more robust synthetic materials that are more readily integrated into practical devices. So far, the guided etching of polymer films, focused ion-beam sculpting, and electron-beam lithography and tuning of silicon nitride membranes have emerged as three promising approaches to define synthetic solid-state pores with sub-nanometre resolution. These procedures have in common the formation of nominally cylindrical or conical pores aligned normal to the membrane surface. Here we report the formation of 'kinked' silica nanopores, using evaporation-induced self-assembly, and their further tuning and chemical derivatization using atomic-layer deposition. Compared with 'straight through' proteinaceous nanopores of comparable dimensions, kinked nanopores exhibit up to fivefold reduction in translocation velocity, which has been identified as one of the critical issues in DNA sequencing. Additionally, we demonstrate an efficient two-step approach to create a nanopore array exhibiting nearly perfect selectivity for ssDNA over dsDNA. We show that a coarse-grained drift-diffusion theory with a sawtooth-like potential can reasonably describe the velocity and translocation time of DNA through the pore. By control of pore size, length and shape, we capture the main functional behaviours of protein pores in our solid-state nanopore system.

Pioneering work demonstrating single-channel recordings of ionic transport through biological ion channels reconstituted in synthetic 'black lipid membranes' has provoked considerable recent interest in the fabrication of synthetic pore-channel systems intended to mimic their biological counterparts. In nature, integral membrane protein channels formed by self-assembly control the trafficking of ions and molecules into and out of the cell and between the cytosol and subcellular organelles. More than a decade ago, it was demonstrated that the biological pore-forming protein alpha-haemolysin, with pore-aperture diameter of 1.4 nm, exhibits selective voltage-driven transport of ssDNA, while preventing transport of the larger (~2-nm-diameter) dsDNA. Because voltage-driven DNA translocation partially occludes the pore, it reduces by an order of magnitude the accompanying ion current, allowing detection of single-molecule translocation events in a manner similar to Coulter counting¹. Furthermore, because each base pair is expected to have different pore-blocking characteristics, it has been proposed that the modulation of the ion current during translocation could be used to directly sequence DNA.

Despite their advantages of genetically controlled pore size and topology, natural protein channels reconstituted in free-standing fluid lipid bilayers are fragile and thus not suitable for integration into high-throughput technologies. For this reason, solid-state nanopores are currently under extensive evaluation. Compared with proteins, solid-state nanopores are mechanically robust, can tolerate and operate over a broader range of temperature, pH and chemical conditions and, potentially, could be integrated

into practical analytical devices or platforms. So far, solid-state nanofabrication approaches have demonstrated precise tuning of pore size over the range from 1 to over 10 nm (refs 2–5). However, fabrication of these channels generally requires the resizing of pores with ion/electron beams, especially as the pore size approaches the nanometre level. Therefore, an array of nanopores is typically fabricated 'one at a time' with smooth, nominally cylindrical or conical side walls oriented normal to the membrane surface. As an alternative approach to solid-state nanopore fabrication, we report here a silica-surfactant self-assembly approach to create an array of nanopores suspended over a silicon nitride aperture. Using a non-ionic surfactant to direct the formation of a porous silica mesophase, we form a periodic pore-network array with pore orientations that deviate periodically from the surface normal. Atomic-layer deposition is used subsequently to adjust the pore diameter from 2.6 to 1.4 nm as well as altering the surface chemistry. We find that these kinked nanopores reduce the translocation velocity up to fivefold compared with comparably sized straight-through pores. Reducing DNA translocation speed during detection is important for polymer identification and sequencing in nanopores^{6–8} and has been demonstrated by control of external factors such as solution composition and operation conditions in both biological and solid-state straight-through nanopore systems^{9,10} as well as by use of optical tweezers¹¹. In contrast, here we show that a kinked nanopore array system fabricated by self-assembly can slow down DNA translocation speed through its unique pore morphology alone.

¹Department of Chemical & Nuclear Engineering and Center for Micro-Engineered Materials, University of New Mexico, 87131, USA, ²Sandia National Laboratories, 87185, USA, ³School of Pharmacy, University of New Mexico, 87131, USA, ⁴Department of Mechanical Science and Engineering and Beckman Institute for Advanced Science and Technology, University of Illinois at Urbana-Champaign, 61801, USA, ⁵School of Chemical Engineering, Purdue University, 47907, USA, ⁶Department of Molecular Genetics and Microbiology, The University of New Mexico, 87131, USA. *e-mail: cjbrink@sandia.gov.

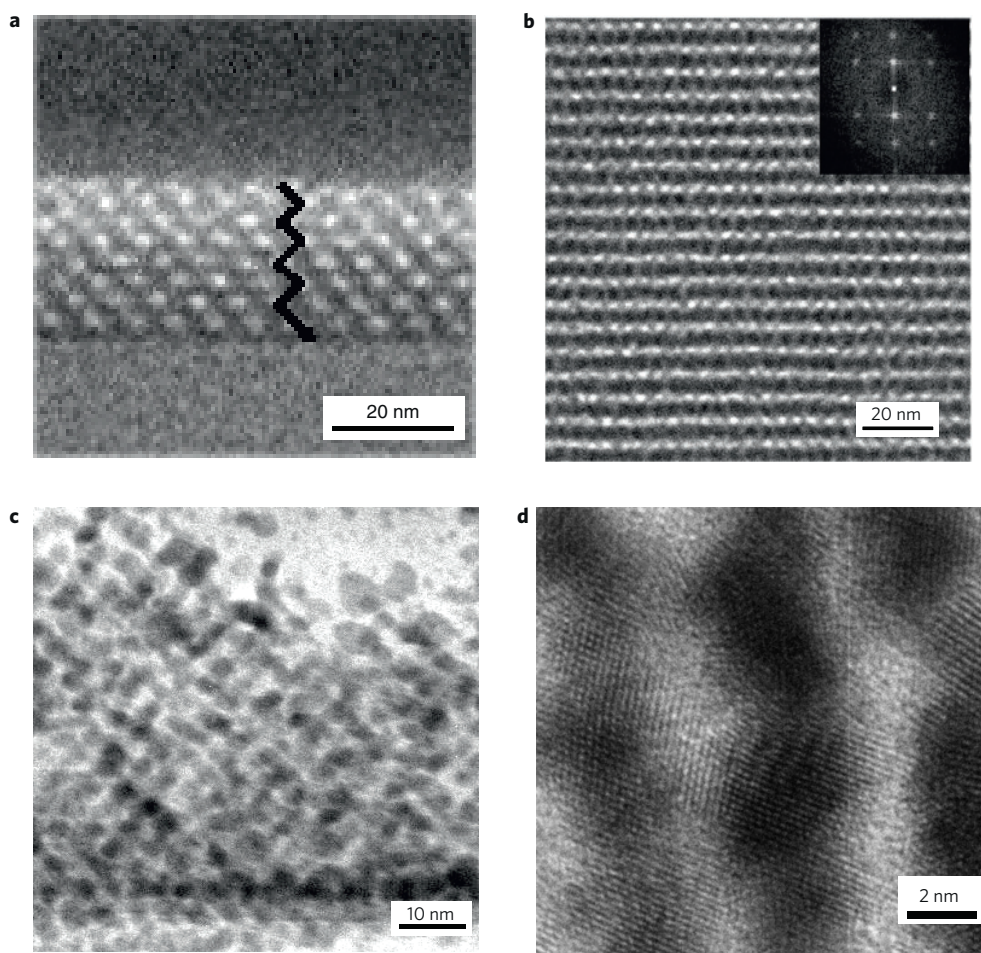


Figure 1 | TEM images of porous and Pt pore-filled thin-film mesophases. **a**, TEM cross-sectional image along [110] for an *Fmmm* mesoporous film, deposited on an oxidized silicon substrate and calcined at 400 °C, suggesting a kinked pore pathway through the film. **b**, TEM plan-view image along [001] of the same ultrathin nanoporous silica film as in **a**; the inset contains a fast Fourier transform of the bright-field image. **c**, Cross-sectional image along [110] of a Pt replica network after electrochemical deposition of Pt inside the porous film, consistent with the cross-sectional image in **a**. **d**, High-resolution cross-section image of the Pt replica, showing the crystalline structure of the deposited Pt.

Nanopore-array fabrication

Free-standing arrays of silica nanopores spanning circular ~50–100-nm-diameter apertures, defined in silicon nitride by focused ion-beam (FIB) lithography, were fabricated by evaporation-induced self-assembly (EISA; refs 12–14), employing the non-ionic surfactant Brij 56 as a structure-directing agent. EISA starts with a homogenous alcohol–water solution of hydrophilic silicic acid precursors plus surfactant. Evaporation accompanying dip-, spin- or aerosol coating progressively concentrates the depositing film in non-volatile silica and surfactant components, resulting in self-assembly of micelles and further self-organization into periodic three-dimensional, silica–surfactant mesophases oriented with respect to the substrate and vapour interfaces. Originally developed to coat solid substrates, we have extended EISA to the formation of free-standing films spanning ~50–100-nm-diameter pores through spin-coating or aerosol deposition¹⁵. Using cationic and non-ionic surfactants and block copolymers, a variety of cubic and bicontinuous thin-film mesophases have been developed (for example, three-dimensional hexagonal *P6₃/mmc* (ref. 16), micellar cubic (face-centred cubic and body-centred cubic, bcc)^{17,18} and bicontinuous cubic (double gyroid and so on)¹⁹). These structures are of interest for membranes because they have the potential to create the three-dimensional pore connectivity needed for transmembrane permeation. Previous work in our group used Brij 56 under acidic conditions to direct the formation of

supported cubic nanoporous silica membranes characterized by an *Im $\bar{3}m$* body-centred symmetry and a Barrett–Joyner–Halenda (BJH) pore diameter of approximately 2.6 nm (ref. 18). Here, to achieve thinner films more commensurate with the dimensions of natural membrane systems, we adopted the same recipe but diluted eightfold in ethanol, yielding the final Si : Brij 56 : EtOH : HCl : H₂O molar ratio 1.28 : 0.076 : 248 : 0.09 : 71. As shown by the transmission electron microscopy (TEM) cross-sectional image (Fig. 1a), spin-coating this composition at 1,000 r.p.m. followed by calcination at 400 °C results in highly ordered films only ~30 nm thick. With regard to DNA translocation, thin films are important because: (1) a shorter contour length increases the likelihood that the channel is continuous and spans the membrane; (2) decreased thickness provides a greater field strength within the membrane, thereby imparting greater momentum to the DNA in overcoming the potential of mean force needed to translocate the pore; (3) modification of the pore surface by post-grafting or atomic-layer deposition (ALD) becomes more efficient when the contour length of the channel is shorter.

Grazing-incidence small-angle X-ray scattering (GISAXS) was used to characterize the structure of the periodic thin-film mesophase. In GISAXS, an X-ray beam is incident on a sample at an angle greater than the critical angle of the film but less than that of the substrate (typically about 0.2°), maximizing the scattering volume of the beam within the film. Use of

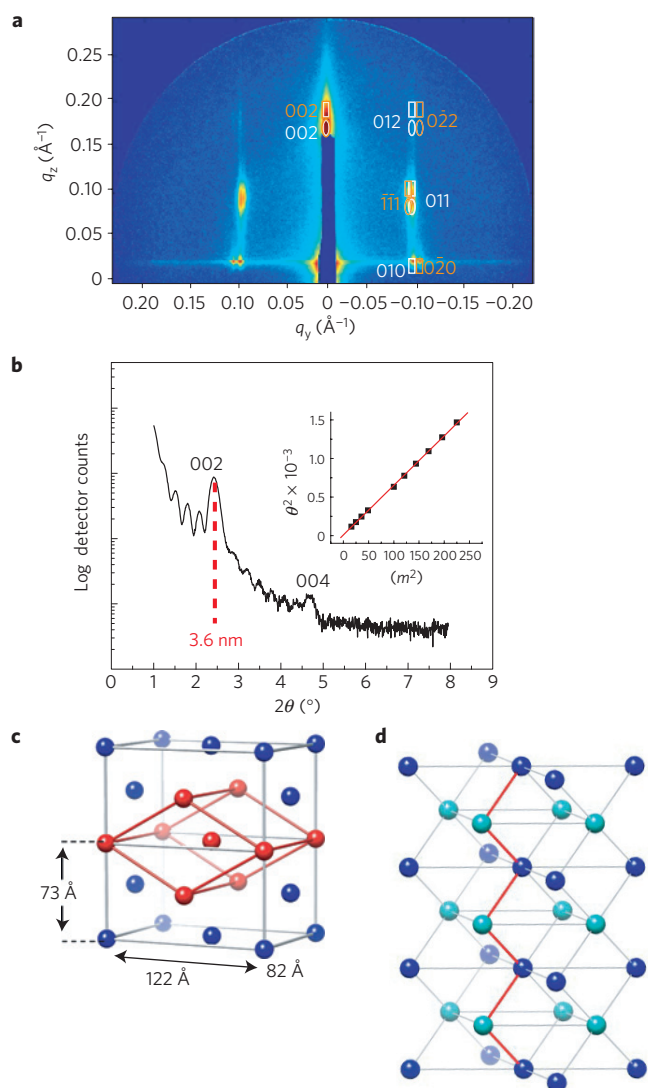


Figure 2 | X-ray scattering analyses and corresponding structure of the ordered, porous, silica thin-film mesophase membrane used for the DNA-translocation experiments. **a**, Typical two-dimensional GISAXS data for a self-assembled porous silica film (about 30 nm thick) as used for DNA-translocation experiments, showing the presence of two phases, described by *Fmmm* (in orange) and *P6₃/mmc* (in white) symmetry. Unit-cell parameters are given in the text. Ovals and rectangles signify the predicted positions of diffraction from the incident and reflected beams, respectively. **b**, XRD data collected on the same film as analysed in **a**, showing Bragg reflections consistent with the GISAXS data as well as interference fringes arising from the extreme thinness of the film. The inset shows the plot of m^2 versus θ^2 used to estimate the film thickness, with m being the reflection order and θ the diffraction angle in degrees. **c**, Two unit cells of the *Fmmm* phase, showing the unit-cell dimensions determined from the fit to the GISAXS data in **a** as well as the relationship of *Fmmm* to the 'distorted' *Im3m* unit cell (shown in red). **d**, Schematic of the [001]-oriented *Fmmm* phase, showing lattice points (here representing the positions of pores) in alternate planes signified by colour and the eightfold coordination characteristic of bcc packing indicated by grey lines. The shortest kinked pathway through the lattice is labelled in red.

a two-dimensional detector enables collection of both in- and out-of-plane scattering data for comparison of the pattern to a hypothesized nanostructure²⁰. Figure 2a contains typical GISAXS data for an about 30 nm film synthesized in an identical manner to the films used for DNA-translocation experiments. We find

data consistent with the presence of two separate but related mesophases: a [001]-oriented face-centred orthorhombic phase with unit-cell parameters $a = 82 \text{ \AA}$, $b = 122 \text{ \AA}$ and $c = 73 \text{ \AA}$; this unit cell is an equivalent description of a [110]-oriented *Im3m* (bcc) phase with $a = 82 \text{ \AA}$, contracted by about 37% in the direction perpendicular to the substrate from uniaxial film shrinkage^{21,22}, and a [001]-oriented three-dimensional hexagonal *P6₃/mmc* with unit-cell parameters $a = b = 67 \text{ \AA}$ and $c = 73 \text{ \AA}$. The in-plane domain size was estimated through line-width analysis to be 200 nm and 125 nm for the *Fmmm* and *P6₃/mmc* phases, respectively. These unit-cell parameters, along with typical Brij 56 micelle dimensions (about 4–5 nm), conform to the existence of micellar-type (as opposed to minimal-surface) bcc and hexagonally close-packed mesophases; we note that these two phases are closely related through a simple diffusionless transformation (see Supplementary Information for more details, along with GISAXS analysis of a thicker Brij 56 templated film). XRD data (Fig. 2b) shows only one set of Bragg peaks (with interplanar spacing $d = 36 \text{ \AA}$), reinforcing the presence of identical interplanar spacing for both structures found inside this film. Also present in the XRD data are Kiessig fringes, from which a film thickness of 28 nm can be calculated (Fig. 2b, inset) for the film after template removal, consistent with TEM and ellipsometric measurements.

Figure 2c,d contains an illustration of the *Fmmm* unit cell (c), as well as a schematic of the overall DNA-translocation pathway through the film (d). Although the precise shape and connectivity of pores within the film is not known, we place a sphere at each lattice point of the *Fmmm* structure that corresponds to bcc packing to represent the likely positions of pores, and connect these pores in d using the standard eightfold bcc coordination of each lattice point. The shortest pathway through the film, highlighted in red, presents a tortuosity of about 1.5 (the whole pore length divided by film thickness). DNA translocation through other pathways is unlikely, as the electric field is strongest in this direction. Also, pore connectivity of pathways parallel to the plane of the film may be limited owing to larger pore-to-pore spacing. The related hexagonally close-packed structure (Supplementary Information) has the same tortuosity of about 1.5, indicating that DNA passes through an identical pore length through the film thickness in both *Fmmm* and *P6₃/mmc* mesophases.

Figure 1a,b contains the TEM cross-sectional and plan-view images of a film prepared in an identical manner to the film analysed in Fig. 2. The plan view in Fig. 1b shows the (001) plane of the *Fmmm* structure; the unit-cell parameters a and b calculated from the fast Fourier transform (see the inset) are 8.4 nm and 12.1 nm respectively, consistent with results simulated from GISAXS data. Moreover, the a/b ratio is close to the $1 : \sqrt{2}$ in-plane ratio that is described by the (001) plane of our *Fmmm* thin-film structure^{21,22}. Consistent with GISAXS analysis, plan-view TEM images of hexagonal (the (001) plane of *P6₃/mmc*) or mixed packing were also observed (see Supplementary Fig. S2). The cross-section in Fig. 1a shows the (110) plane of the *Fmmm* structure, with an overall film thickness of about 30 nm (the most likely tortuous pore pathway through the film is highlighted in black). N₂ adsorption, acquired directly on a thin film using a surface acoustic wave technique²³ (see Supplementary Fig. S1), shows a typical type IV isotherm; the average BJH pore diameter calculated from these data is 2.6 nm.

Considering the inaccuracy of BJH methods in estimating pore dimensions in such a small pore-size range and the fact that cubic or three-dimensional hexagonal networks derived from micellar mesophases such as those in our ultrathin films are expected to have undulating pore diameters along the pore pathway, we applied an electrochemical approach to create a Pt replica of the nanopore network as a means to better estimate pore size and to examine the pore connectivity across the film. Figure 1c shows a TEM

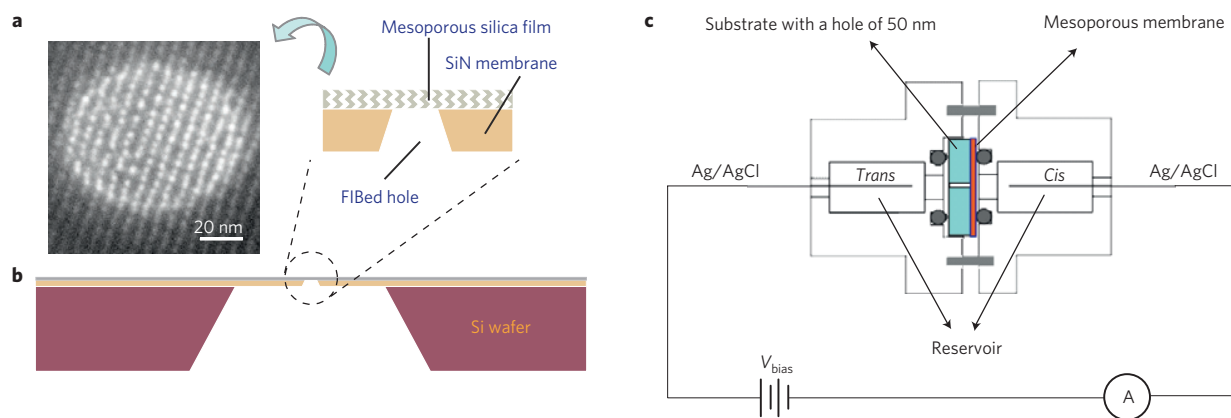


Figure 3 | Experimental platform for monitoring DNA translocation through a freely suspended kinked nanopore membrane. **a**, TEM plan-view image of a free-standing *Fmmm* film suspended over a sub-100-nm-diameter aperture formed by FIB. The orientation is along [001]. **b**, Schematic of the experimental platform showing the free-standing film suspended over an aperture formed in a silicon nitride window by FIB. Nanopores are tortuous in the direction normal to the film surface. **c**, Schematic of the electrochemical cell for carrying out voltage-driven DNA-translocation experiments.

cross-sectional image of the resulting Pt replica formed within the original *Fmmm* silica framework structure along [110]. The presence of a well-defined Pt network indicates pore connectivity with a tortuous shape for the pore pathway that transverses the film. High-resolution TEM of the Pt replica (Fig. 1d) shows crystalline lattice fringes of Pt with alternating wide and narrow regions corresponding to templated pores and the necking between them, respectively, giving estimated dimensions of about 4 nm for the pore diameter and about 2.6 nm for interpore necks. This suggests that pore-to-pore connectivity provides the transport-limiting barrier to DNA translocation. Therefore, we assign 2.6 nm as the ‘effective pore diameter’ to refer to the transport-limiting pore dimension. Additionally, the cross-sectional TEM image of the Pt replica in Fig. 1d suggests preferential pore-to-pore connectivity in the through-thickness direction, whereas pore connectivity within the plane is limited.

As shown in Fig. 3a, spin-coating exactly the same composition as in Figs 1 and 2 over a ~ 80 -nm-diameter aperture (formed in silicon nitride by FIB as shown schematically in Fig. 3b; ref. 24) results in an array of ordered nanopores freely suspended over the aperture. Figure 3c shows integration of the free-standing nanopore array in a home-built electrochemical cell for carrying out DNA-translocation experiments. As discussed above, our self-assembled nanopores are in a similar size range as those reported in previous studies of DNA translocation. However, the mesophase symmetry of our ultrathin film structure requires that there are no straight-through pores spanning the membrane, allowing us to isolate and understand the influence of nanopore tortuosity on DNA translocation.

Atomic-layer deposition (ALD)

To reduce the effective nanopore dimension below 2.6 nm and to modify the pore surface chemistry, we carried out thermal ALD of titania or an aminosilane (operational procedures and set-up reported elsewhere²⁵). ALD is a self-limiting, highly conformal, layer-by-layer deposition process composed of two half-cycles, hydrolysis and condensation. For a hydroxylated surface like that of a silica nanopore, condensation is achieved by exposure to a halide or alkoxide precursor, resulting in Si–O–M bond formation and concomitant reduction in the pore diameter. To trigger another layer of deposition, water is introduced to the system, resulting in hydrolysis of surface bonds. Table 1 lists refractive-index data measured by spectroscopic ellipsometry for thin nanoporous silica films before and after one and two layers of thermal TiO₂ ALD, and the corresponding volume

Table 1 | Refractive index, pore volume fraction and TiO₂ volume fraction calculated using a Bruggeman effective-medium approximation, and the corresponding thickness of TiO₂ and pore-size reduction (σ) for one and two layers of TiO₂ ALD deposition inside a silica nanopore film.

	Refractive index	Pore volume fraction	Volume fraction of TiO ₂	TiO ₂ thickness (Å)	σ (Å)
Before ALD	1.260	0.42	–	–	–
1 Layer TiO ₂ ALD	1.305	0.37	0.05	1.7	3.4
2 Layer TiO ₂ ALD	1.350	0.33	0.09	3.2	6.4

percentage and thickness of TiO₂ calculated from this data using a Bruggeman effective-medium approximation²⁶ (calculated using $n_{\text{SiO}_2} = 1.46$ and $n_{\text{TiO}_2} = 2.00$), in combination with Brunauer–Emmett–Teller film surface areas obtained from N₂ adsorption data (290 m² g^{−1} for the film before ALD, and 286 m² g^{−1} after one layer of ALD). Although the estimated volume fraction of TiO₂ is dependent on the value of the refractive index for TiO₂ used in the effective-medium approximation calculations, variation of n_{TiO_2} over the range of 1.90–2.10 (typical for non-crystalline titania) modifies the volume fraction by only about 10%. The calculated thicknesses of 1.7 Å for the first ALD layer and 1.5 Å for the second layer are consistent with the expected thickness per deposition step of about 1.6 Å (ref. 27), indicating that one and two layers of TiO₂ ALD deposition inside the silica nanoporous film result in pore-diameter reductions of approximately 3.4 and 6.4 Å respectively. Therefore, for our original thin film with a 2.6 nm ‘effective pore diameter’ determined by the BJH calculation in combination with high-resolution TEM of the Pt replica, the approximate pore diameters after one and two layers of TiO₂ ALD are 2.3 nm and 2.0 nm respectively. Also, the BJH pore diameters calculated from the N₂ adsorption isotherm before and after one layer of ALD show about 3 Å decrease of pore diameter (see Supplementary Fig. S5), which is close to that calculated from the refractive-index data (Table 1); although the BJH method can be subject to large errors in the determination of absolute pore size, errors in relative measurements are expected to be significantly lower.

We also used ALD to form a coherent aminopropyl silane monolayer using the molecular precursor aminopropyl trimethoxysilane (APTMS). Successive cycles of APTMS and

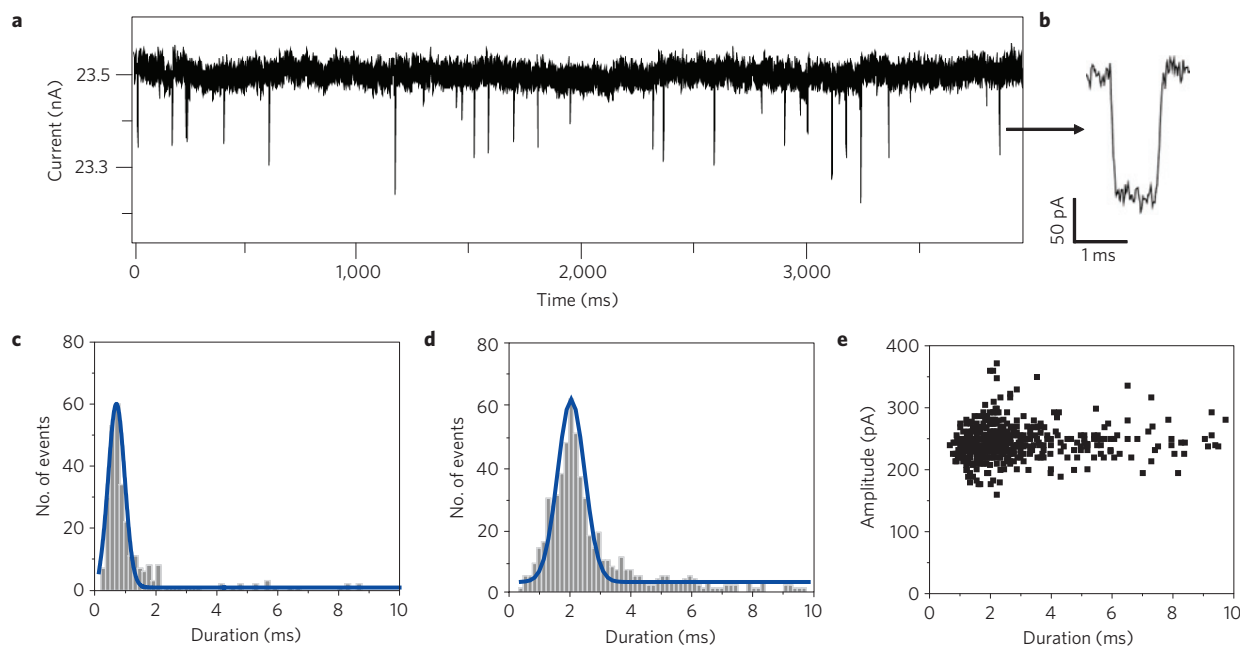


Figure 4 | Analysis of DNA translocation through a kinked-nanopore array. **a**, A typical trace of current as a function of time during dsDNA translocation, showing a series of current blockages. **b**, Magnification of a single current blockage event. **c**, Duration histogram of 2.7-kbp DNA translocation events for a 2.6-nm-diameter silica nanopore array. **d**, Duration histogram of 2.7-kbp DNA translocation events for the silica nanopore array as in **c** after one cycle of thermal TiO₂ ALD, which reduces the pore diameter to about 2.3 nm. **e**, A typical event scatter diagram of amplitude and duration for 560 current-blockage events for the nanopore array after 1 cycle of TiO₂ ALD as in **d**. The applied voltage is 200 mV for all experiments. Events with duration longer than 10 ms were also observed but not shown in the histogram.

H₂O favour condensation reactions between alkoxy silane groups on APTMS and silanol groups on the pore surface or between alkoxy silane groups of nearby APTMS, resulting in an aminopropyl silane monolayer as opposed to a multilayer²⁸. The Fourier-transform infrared spectrum (Supplementary Fig. S6) after one cycle of APTMS/H₂O shows that two new vibrational bands appear, attributable to N–H bending (scissoring) of primary amines (around 1,650 cm⁻¹) and C–H stretching of alkyl chains (around 2,900 cm⁻¹) respectively, consistent with the formation of an APTMS monolayer.

DNA translocation

A representative ionic-current-versus-time trace for voltage-driven dsDNA translocation through a 2.6-nm-diameter silica nanopore array is shown in Fig. 4a (see Methods for a detailed description of the set-up and experimental procedure). In this experiment, 2,700-base-pair (2.7-kbp) dsDNA was introduced to the *cis* side of the cell and a potential of +200 mV was applied to the *trans* side. A series of current-blockage events is observed. Reversing the voltage bias or replacing dsDNA with blank buffer solution suppressed all current-blockage events, implying that the observed blockages are caused by dsDNA translocation. The background current (~23,000 pA) represents the collective ion current through all the nanopores on the aperture (estimated to be ~80 pores in this case). Correspondingly, it is greater than that of a single-nanopore system^{29–31} and scales with the size of the aperture and number of pores in the array. However, the current-blockage amplitude (~200 pA @200 mV) per event is comparable to that reported previously for single nanopores³². We claim that each current blockage represents a single event of one dsDNA molecule passing through an individual pore, and the overall current-blockage frequency is the sum of the dsDNA translocation events on all nanopores supported over the FIBed aperture. Because the translocation time τ (<1 ms) is short compared with the event frequency (0.5–1 s/event), the probability of two events coinciding

is very rare, implying that in our array dsDNA translocation characteristics of individual pores can still be detected and interpreted as for single-nanopore systems.

Figure 4c shows that the most probable dsDNA translocation time τ in 2.6 nm pores is 0.7 ms, corresponding to a velocity of 1.3 mm s⁻¹, calculated from $v = L_{\text{DNA}}/\tau$ (refs 32,33), in which L_{DNA} is the polymer length, almost an order of magnitude less than that reported elsewhere using larger solid-state nanopores^{9,30,32,33}. One cycle of TiO₂ ALD reduces the pore diameter by ~0.3-nm (to ~2.3-nm) and further reduces the velocity by about a factor of three (~0.45 mm s⁻¹) (Fig. 4d). This large dependence of velocity on pore size is consistent with a strong polymer–pore interaction^{34–36} (see further discussion below). Figure 5a shows that the translocation time τ scales linearly with polymer length l . According to the analysis in ref. 37, if hydrodynamic friction within the pore dominates the transport dynamics, the constant driving force F experienced by the polymer within the pore ($F = 2eV/a_0$, where e is the elementary charge, V is the potential difference and a_0 (= 0.4 nm) is the spacing between nucleotides) is balanced by the hydrodynamic friction within the pore = $\xi_{\text{eff}}v$, where, ignoring any specific DNA–pore interactions, $\xi_{\text{eff}}v = 2\pi\eta L_{\text{pore}}rv/(R-r)$ (where R is the pore radius, r is the dsDNA cross-sectional radius, η is the solvent viscosity, L_{pore} is the pore length and v is the linear velocity of the polymer inside the pore). This implies the translocation velocity v to be constant with polymer length, as we observe. Additionally, because ALD deposition is conformal and changes the pore size but not its shape, we can use the force balance to estimate the velocity ratio v_1/v_2 in reducing the pore radius from R_1 to R_2 at a constant driving potential. Reducing $2R$ from 2.6 to ~2.3 nm (Table 1) should reduce v by a factor of about two. Experimentally, we observe a factor of three, suggesting additional frictional forces arising from specific polymer–pore interactions or, more likely, the tortuous pore shape defined by the micellar mesophase³⁷. A second cycle of TiO₂ ALD reduces the pore diameter to 1.9–2.0 nm, below that of dsDNA, and, as expected, we observe no measurable dsDNA

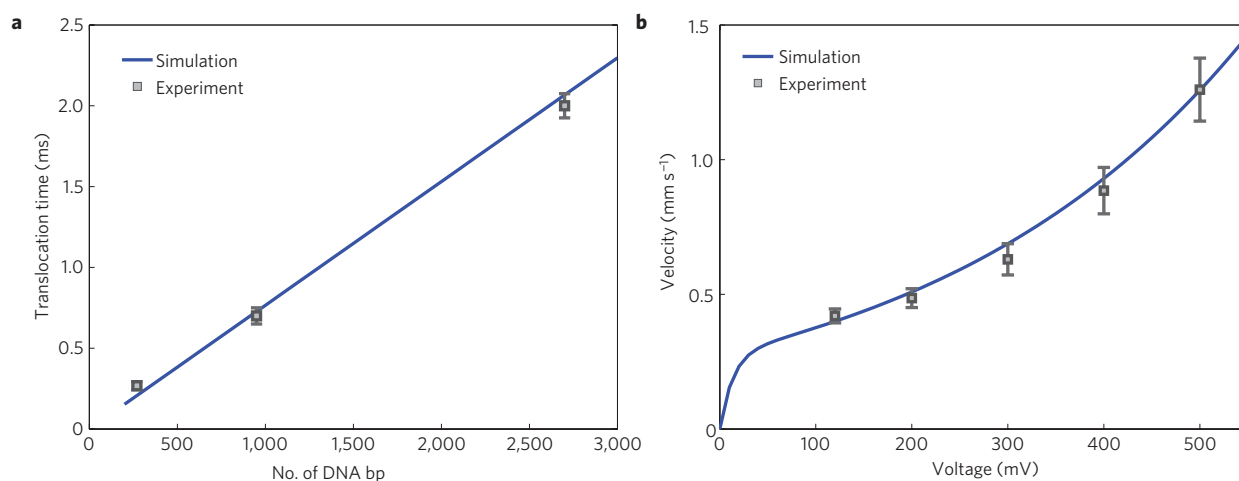


Figure 5 | Dynamics of dsDNA translocation through a kinked-nanopore array. **a**, Dependence of translocation time of dsDNA on size (270 bp, 950 bp and 2.7 kbp). **b**, Translocation velocity as a function of applied voltage for 950-bp dsDNA. The error bars denote standard deviation evaluated from dwell-time histograms. Simulated data are based on a one-dimensional drift-diffusion model, as described in the text.

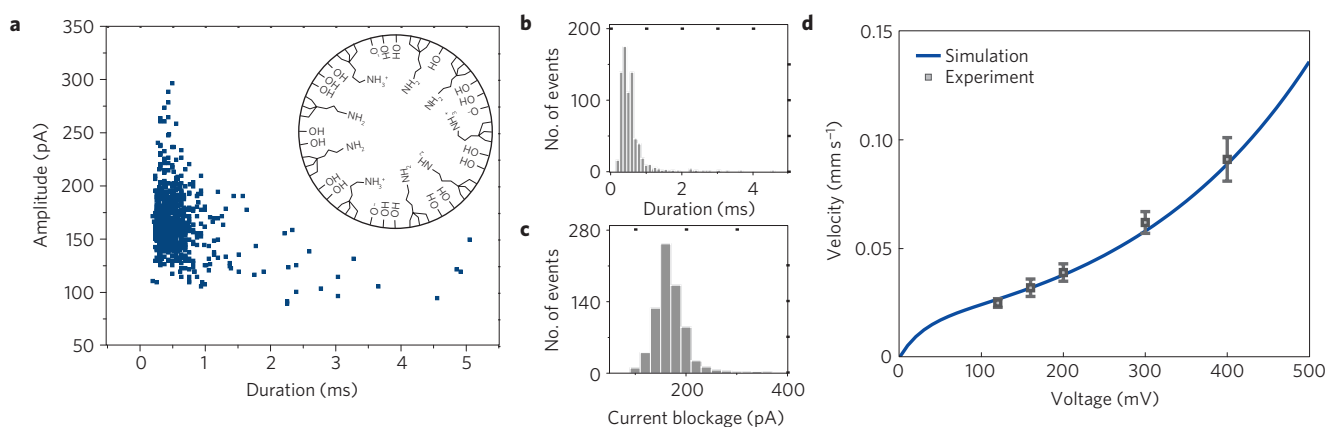


Figure 6 | Analysis of ssDNA translocation through a kinked-nanopore array after APTMS ALD treatment. **a–c**, Event diagram of poly(dA)₁₀₀, given -400 mV on the *cis* side (**a**) and the corresponding duration histogram (**b**) and current-blockage histogram (**c**). The inset of **a** shows a hypothetical schematic of the pore cross-section after successive ALD half-cycles of APTMS and water. **d**, Poly(dA)₁₀₀ translocation velocity as a function of applied voltage for the APTMS-modified pore. The error bars denote the standard deviation evaluated from dwell-time histograms. Simulated data are based on a one-dimensional drift-diffusion model, as described in the text.

translocation (for driving potentials less than 500 mV where we expect there to be no denaturation). A final dynamical feature of our nanopore system is the approximate quadratic relationship between velocity and voltage (Fig. 5b).

The transport characteristics of the kinked-nanopore arrays we describe above are distinct from those of other solid-state nanopores^{36,37} and more similar to protein nanopores. For example, the authors of ref. 37 observe the translocation time in 10-nm-diameter solid-state nanopores to vary with dsDNA length as a power law, $\tau \sim l^{1.27}$, which they attribute to the condition where hydrodynamic drag imposed by the untranslocated polymer on the *cis* side dominates the friction within the pore. In fact, they conclude that the essential difference between solid-state and protein pores is that, for sufficiently shallow solid-state pores, the effect of friction within the pore is negligible. In comparison, for ssDNA translocation through α -haemolysin^{34,38,39} the translocation time was found to vary linearly with polymer length, consistent with pore-friction-dominated translocation owing to the small 1.4-nm-diameter pores plus possible specific DNA–pore interactions.

To more closely emulate the behaviour of protein pores in our solid-state system, we modified the 2.6 nm silica nanopores with APTMS (see the schematic in the inset of Fig. 6a). On

the basis of ellipsometric measurements of the thickness of the corresponding film deposited by ALD on a solid silica support, we estimate that one layer of APTMS reduces the pore diameter to about 1.4 nm, comparable to that of α -haemolysin. Additionally, the partial positive surface charge of the aminopropyl groups (NH_3^+) introduces an attractive electrostatic DNA–pore interaction, a factor that has been reported to enhance DNA translocation⁴⁰.

For the APTMS-modified nanopore array, no current blockages were observed for 2.7-kbp dsDNA. For pure poly(dA)₁₀₀ current-blockage events were observed, and the corresponding translocation times and current blockages are shown in the histograms in Fig. 6b,c. When poly(dA)₁₀₀ was added to 2.7-kbp dsDNA, current blockages were again observed and the duration and current-blockage histograms were similar to those of pure poly(dA)₁₀₀. Polymerase chain reaction (PCR) analysis verified dsDNA translocation in the original nanopore array with about 2.6 nm pore diameter, but rejection in the APTMS-modified nanopore array with about 1.4 nm pore diameter; ssDNA translocation was verified in both cases, consistent with the observation of translocation events from current blockage (see Supplementary Fig. S8). These results strongly suggest: (1) with APTMS-modified nanopores, separation of ssDNA from dsDNA is achieved and can

be sensed electronically; (2) pore-size reduction by ALD occurs uniformly for all pores, allowing selectivity to be developed in an array format. Recently, great effort has been made to distinguish single- and double-stranded nucleic acid molecules using solid-state nanopores^{41,42}. Our results, showing nearly perfect selectivity for ssDNA over dsDNA in ALD-modified nanopores, could expand the range of potential applications of synthetic solid-state nanopores in biotechnology by tuning the pore size to be between the diameters of dsDNA and ssDNA.

Figure 6d shows the velocity of poly(dA)₁₀₀ as a function of applied voltage in the APTMS-modified nanopore array. The velocity was calculated from the blockade-duration half-life τ (the time over which the current blockage increases and decreases by 50% of its maximum value) according to L_{DNA}/τ , which is the appropriate relation for the condition where the polymer length $L_{\text{DNA}} \cong$ the pore length L_{pore} (film thickness (30 nm) \times tortuosity (1.5); ref. 34). We observe an approximate quadratic relationship between velocity and applied voltage similar to that reported for poly(dA) translocation through α -haemolysin^{34,43}. However, direct comparison of the translocation time of poly(dA)₁₀₀ through the APTMS-modified nanopore and α -haemolysin under identical conditions (22 °C, 120 mV; ref. 44) shows ~ 5 times longer translocation times (1.6 ms compared with 0.3 ms) and, correspondingly, ~ 5 times lower velocity for the APTMS-modified nanopore. As the pores are of comparable diameters, we attribute this difference to the more tortuous shape of our solid-state nanopore, most likely owing to a higher energy barrier derived from the pore kinkedness. Our transport model further verifies the higher energy barrier in our tortuous nanopores compared with that in straight-through pores and clearly explains the physical characteristics of the parameters used in the simulation, with values that can all be well explained by strong interaction between the polymer and the kinked pores.

Transport model

The distinguishing transport characteristics of our kinked nanopore array, namely, linear dependence of translocation time on polymer molecular weight and quadratic dependence of translocation velocity on voltage, shared additionally by protein pores, are captured by a one-dimensional drift–diffusion model³⁵:

$$\frac{\partial P}{\partial t} = D_0 \frac{\partial}{\partial x} \left[\frac{\partial P}{\partial x} + \frac{1}{k_B T} \frac{\partial \Phi}{\partial x} P \right] \quad (1)$$

where $P(x, t)$ is the probability that a length x of the polymer's backbone has passed through the pore at time t , D_0 is the diffusion coefficient, assumed to be $10^{-8} \text{ cm}^2 \text{ s}^{-1}$ owing to the confined environment⁴⁵, and T is the temperature. Φ is the potential owing to the various interactions of the polymer with the pore and the applied voltage drop. The potential Φ is approximated by the expression

$$\Phi(x) = U(x) - Fx \quad (2)$$

where F is determined by the applied voltage drop, and $U(x)$ represents the polymer's interactions with the pore. $U(x)$ is assumed to be a sawtooth-like potential, which is described by two dimensionless parameters, the peak height, $U_0/k_B T$, and the asymmetry parameter, α . The value of α depends on several factors including the pore geometry and U_0 is the energy barrier DNA must overcome for translocation, represented by the height of the sawtooth-like potential, which also depends on several factors including the pore geometry and is typically of the order of several $k_B T$.

In the case of a strong polymer–pore interaction (characterized by a large U_0), where diffusion can be described as hopping

from one potential minimum to the next potential minimum, an approximate expression for the polymer velocity, v , can be obtained from equations (1) and (2) as³⁵

$$v \approx \frac{D_0}{a_0 I_1^{(0)} I_2^{(0)}} \left[\exp\left(\frac{\alpha F a_0}{k_B T}\right) - \exp\left(-\frac{(1-\alpha) F a_0}{k_B T}\right) \right] \quad (3)$$

where

$$I_1^{(0)} = \int_0^{a_0} \frac{1}{a_0} \exp\left(\frac{U(x)}{k_B T}\right) dx \quad \text{and} \quad (4)$$

$$I_2^{(0)} = \int_0^{a_0} \frac{1}{a_0} \exp\left(\frac{-U(x)}{k_B T}\right) dx$$

In our calculations for dsDNA, we assume $a_0 = 4 \text{ \AA}$, $D_0 = 10^{-12} \text{ m}^2 \text{ s}^{-1}$, $U_0 = 5.7 k_B T$ and $\alpha = 0.04$. Using these parameters, we compute the average velocity using equations (3) and (4). The translocation time is then computed using the expression $\tau = L_{\text{DNA}}/v$, where L_{DNA} is the length of the DNA chain. In Fig. 5 we compare our experimental results with predictions made by the one-dimensional drift–diffusion model for dsDNA. We repeated the calculations for the poly(dA)₁₀₀ case using $a_0 = 4 \text{ \AA}$, $U_0 = 9.7 k_B T$ and $\alpha = 0.11$. The calculations are compared with the experimental data in Fig. 6d. In the literature, U_0 has been assumed to vary from 0 to $10 k_B T$ and α is assumed to vary from 0 to 1, where $\alpha = 0$ when DNA is interacting with a reflecting boundary, and $\alpha = 1$ when the DNA is interacting with an absorbing boundary^{46,47}. Our simulation results show that both U_0 and α values vary as a function of the kinkedness of the pore. For example, when U_0 was taken to be $4.5 k_B T$ in a straight nanopore system results were obtained that reasonably explained the experimental observations⁴⁶. In our simulation, the U_0 value is higher for both dsDNA and ssDNA cases compared with the straight nanopore system. As the DNA–pore interaction is the dominant factor in determining DNA translocation in a small pore^{36,48}, the higher energy barrier can be well explained from the stronger interaction between DNA and the kinked pore. Also, our simulation results show a comparatively low α value. As the reflecting boundary case signifies the inability of the DNA to pass through the pore⁴⁷, our result is consistent with the fact that, as the kinkedness increases, the energy barrier increases, and the surface acts more like a reflecting boundary as the DNA has to adjust its orientation to climb over the wall (the tortuosity of the pore network). It is important to note that, although these parameters are determined from the data of one single experiment, the same values are able to match data from a number of other experiments, suggesting the generality of these parameters for the DNA–nanopore interaction considered in our paper. The close correspondence of the experimental and predicted values emphasizes that nanopore translocation can be adequately (although not explicitly) approximated through assignment of a potential that lumps together the physical and chemical features, pore size, shape, length and interactions, that contribute to pore-friction-dominated transport. It is reasonable to treat the interaction energy between DNA and the nanopore as a sawtooth-like potential. The potential we assumed is physically realistic, being within the range of U_0 values determined by other authors to describe the barrier to permeation of ssDNA through α -haemolysin.

Conclusions

We have demonstrated a simple self-assembly procedure to create a free-standing nanopore array and its further physical and chemical modification by ALD. Compared with lithography or etching,

which yield individual, shallow, straight-through nanopores, self-assembly provides a new means to direct the size, shape and tortuosity of an array of solid-state nanopores. Subsequent conformal ALD of an oxide or silane reduces uniformly the diameters of all pores, enabling, for example, the array to be tuned to transport ssDNA efficiently and reject dsDNA. Compared with protein pores of comparable pore diameters, the greater pore length combined with the kinked pore shape, derived from mixed distorted bcc (with *Fmmm* symmetry) and hexagonally close-packed mesophases, increases the frictional force and reduces the translocation velocity by a factor of up to five. Our approach demonstrates how pore size and shape combine to influence translocation and to address the important issue of reducing translocation speed^{9,11,49}. The qualitative DNA translocation characteristics developed in our nanopore array, for example the linear dependence of translocation time on polymer molecular weight and quadratic dependence of translocation velocity on voltage, can be understood on the basis of a one-dimensional diffusion model, where factors contributing to the frictional force, namely, pore diameter, length, shape and specific interactions, are coalesced into a single barrier potential. We anticipate that future improvements such as integration of our kinked-nanopore array into a three-electrode 'chem-FET' architecture, could combine reduced translocation velocities with increased signal-to-noise ratio, helping the field to realize the goal of direct DNA sequencing.

Methods

GISAXS and electrochemical deposition. GISAXS measurements were made on beamline 8-ID at the Advanced Photon Source at Argonne National Laboratory using a wavelength of 1.6868 Å, a sample-to-detector distance of 1,300 mm and a 2048 × 2048 Marr CCD (charge-coupled device) detector. The angle of incidence was set above the critical angle of the film, but below the critical angle of the substrate; critical angles were measured using X-ray reflectivity on each film sample.

Electrochemical deposition of Pt was carried out by pulsed potentiostatic deposition of a 0.1 M solution of H₂PtCl₆ (duty cycle of 0.000 V versus Ag/AgCl for 5 s followed by -0.300 V versus Ag/AgCl for 10 s) within nanoporous films deposited on a Pt or fluorine-doped tin oxide electrode using the same synthesis procedure as used for producing films for DNA translocation experiments.

DNA translocation set-up. 200-nm-thick Si₃N₄ membranes supported on Si wafers (1 cm × 1 cm × 200 μm thick) with a back-etched 'window' (0.25 mm × 0.25 mm size) were purchased from Structure Probe (SPI) and further drilled with FIB, forming single ~50–100-nm-diameter apertures per window. Nanopore arrays were then deposited by spin-coating, calcination and optionally ALD as described above. Membranes were mounted in an electrochemical cell constructed of Teflon and composed of two separate chambers with capacities up to 1 ml (see Fig. 3c). The Si₃N₄ membrane with the nanoporous array is mounted between the two chambers and sealed with O-rings. Because in the very small-pore system wetting is a critical issue⁵, the film is treated with an oxygen plasma for a short time to fully hydroxylate its surface, and then rinsed in isopropanol for 20 min before mounting the sample in the cell. Ag/AgCl electrodes connected to an amplifier (Axopatch 200B, Axon Instruments, USA) are placed in both chambers to measure the ion current at applied voltages ranging from 120 to 500 mV. Current signal is digitized at 200 kHz (1322A digitizer) and low-pass filtered with a cutoff frequency of 10 kHz. Before making translocation measurements, we wait for the current to become stable.

Size-purified ssDNA was purchased from Midland Certified Reagent and diluted in buffer (10 mM Tris-HCl, 1 mM EDTA, 1 M KCl, pH 8.0) to a concentration of 2 μg ml⁻¹ before loading into the *cis* chamber for DNA translocation experiments. pUC19 plasmid purchased from Biolab was used as template DNA. By digesting the pUC19 plasmid with a specific restriction enzyme at 37 °C for 2 h, we obtained 2.7-kbp linear dsDNA. Additionally, forward and reverse primers were carefully designed to make shorter dsDNA from pUC19, according to the polymerase chain reaction technique. During polymerase chain reaction, a Peltier Thermal Cycler (PTC-200, MJ Research) was used to amplify dsDNA of specific lengths (270 bp and 950 bp); gel electrophoresis was then applied to verify the pure band of DNA with specific length by comparing with the standard bands of a DNA ladder. dsDNA after amplification and digestion are purified (Qiagen purification kits) before use in the experiments. The final dsDNA concentration added to the *cis* side was 2 nM. DNA was stored below -20 °C when not in use. Applied voltages were varied from 120 to 500 mV depending on the experiment.

Received 26 April 2010; accepted 17 June 2010; published online 23 July 2010

References

- Coulter, W. H. Means for counting particles suspended in a fluid. US Patent 2,656,508 (1953).
- Siwy, Z. & Fulinski, A. Fabrication of a synthetic nanopore ion pump. *Phys. Rev. Lett.* **89**, 198103 (2002).
- Li, J. *et al.* Ion-beam sculpting at nanometre length scales. *Nature* **412**, 166–169 (2001).
- Storm, A. J., Chen, J. H., Ling, X. S., Zandbergen, H. W. & Dekker, C. Fabrication of solid-state nanopores with single-nanometre precision. *Nature Mater.* **2**, 537–540 (2003).
- Ho, C. *et al.* Electrolytic transport through a synthetic nanometre-diameter pore. *Proc. Natl Acad. Sci. USA* **102**, 10445–10450 (2005).
- Branton, D. *et al.* The potential and challenges of nanopore sequencing. *Nature Biotechnol.* **26**, 1146–1153 (2008).
- Dekker, C. Solid-state nanopores. *Nature Nanotech.* **2**, 209–215 (2007).
- Nakane, J. J., Akeson, M. & Marziali, A. Nanopore sensors for nucleic acid analysis. *J. Phys. Condens. Matter* **15**, R1365–R1393 (2003).
- Folger, D., Uplinger, J., Thomas, B., McNabb, D. S. & Li, J. L. Slowing DNA translocation in a solid-state nanopore. *Nano Lett.* **5**, 1734–1737 (2005).
- de Zoysa, R. S. S. *et al.* Slowing DNA translocation through nanopores using a solution containing organic salts. *J. Phys. Chem. B* **113**, 13332–13336 (2009).
- Keyser, U. F. *et al.* Direct force measurements on DNA in a solid-state nanopore. *Nature Phys.* **2**, 473–477 (2006).
- Lu, Y. F. *et al.* Continuous formation of supported cubic and hexagonal mesoporous films by sol gel dip-coating. *Nature* **389**, 364–368 (1997).
- Brinker, C. J., Lu, Y. F., Sellinger, A. & Fan, H. Y. Evaporation-induced self-assembly: Nanostructures made easy. *Adv. Mater.* **11**, 579–585 (1999).
- Grosso, D. *et al.* Fundamentals of mesostructuring through evaporation-induced self-assembly. *Adv. Funct. Mater.* **14**, 309–322 (2004).
- Xomeritakis, G. *et al.* Aerosol-assisted deposition of surfactant-templated mesoporous silica membranes on porous ceramic supports. *Microporous Mesoporous Mater.* **66**, 91–101 (2003).
- Besson, S., Ricolleau, C., Gacoin, T., Jacquiod, C. & Boilot, J. P. A new 3D organization of mesopores in oriented CTAB silica films. *J. Phys. Chem. B* **104**, 12095–12097 (2000).
- Liu, N. G., Assink, R. A., Smarsly, B. & Brinker, C. J. Synthesis and characterization of highly ordered functional mesoporous silica thin films with positively chargeable -NH₂ groups. *Chem. Commun.* 1146–1147 (2003).
- Liu, N. G., Assink, R. A. & Brinker, C. J. Synthesis and characterization of highly ordered mesoporous thin films with -COOH terminated pore surfaces. *Chem. Commun.* 370–371 (2003).
- Urade, V. N., Wei, T. C., Tate, M. P., Kowalski, J. D. & Hillhouse, H. W. Nanofabrication of double-gyroid thin films. *Chem. Mater.* **19**, 768–777 (2007).
- Tate, M. P. *et al.* Simulation and interpretation of 2D diffraction patterns from self-assembled nanostructured films at arbitrary angles of incidence: From grazing incidence (above the critical angle) to transmission perpendicular to the substrate. *J. Phys. Chem. B* **110**, 9882–9892 (2006).
- Falcaro, P., Grosso, D., Amenitsch, H. & Innocenzi, P. Silica orthorhombic mesostructured films with low refractive index and high thermal stability. *J. Phys. Chem. B* **108**, 10942–10948 (2004).
- Besson, S., Ricolleau, C., Gacoin, T., Jacquiod, C. & Boilot, J. P. Highly ordered orthorhombic mesoporous silica films. *Microporous Mesoporous Mater.* **60**, 43–49 (2003).
- Ricco, A. J., Frye, G. C. & Martin, S. J. Determination of BET surface-areas of porous thin-films using surface acoustic-wave devices. *Langmuir* **5**, 273–276 (1989).
- Patterson, N. *et al.* Controlled fabrication of nanopores using a direct focused ion beam approach with back face particle detection. *Nanotechnology* **19**, 235304 (2008).
- Jiang, Y. B., Liu, N. G., Gerung, H., Cecchi, J. L. & Brinker, C. J. Nanometer-thick conformal pore sealing of self-assembled mesoporous silica by plasma-assisted atomic layer deposition. *J. Am. Chem. Soc.* **128**, 11018 (2006).
- Khardani, M., Bouaicha, M. & Bessais, B. Bruggeman effective medium approach for modeling optical properties of porous silicon: Comparison with experiment. *Phys. Status Solidi* **4**, 1986–1990 (2007).
- Cameron, M. A., Gartland, I. P., Smith, J. A., Diaz, S. F. & George, S. M. Atomic layer deposition of SiO₂ and TiO₂ in alumina tubular membranes: Pore reduction and effect of surface species on gas transport. *Langmuir* **16**, 7435–7444 (2000).
- Ek, S. *et al.* Atomic layer deposition of a high-density aminopropylsiloxane network on silica through sequential reactions of gamma-aminopropyltriethoxysilanes and water. *Langmuir* **19**, 10601–10609 (2003).
- Heng, J. B. *et al.* The electromechanics of DNA in a synthetic nanopore. *Biophys. J.* **90**, 1098–1106 (2006).

30. Li, J. L., Gershow, M., Stein, D., Brandin, E. & Golovchenko, J. A. DNA molecules and configurations in a solid-state nanopore microscope. *Nature Mater.* **2**, 611–615 (2003).
31. Smeets, R. M. M. *et al.* Salt dependence of ion transport and DNA translocation through solid-state nanopores. *Nano Lett.* **6**, 89–95 (2006).
32. Chen, P. *et al.* Probing single DNA molecule transport using fabricated nanopores. *Nano Lett.* **4**, 2293–2298 (2004).
33. Storm, A. J., Chen, J. H., Zandbergen, H. W. & Dekker, C. Translocation of double-strand DNA through a silicon oxide nanopore. *Phys. Rev. E* **71**, 051903 (2005).
34. Meller, A., Nivon, L. & Branton, D. Voltage-driven DNA translocations through a nanopore. *Phys. Rev. Lett.* **86**, 3435–3438 (2001).
35. Lubensky, D. K. & Nelson, D. R. Driven polymer translocation through a narrow pore. *Biophys. J.* **77**, 1824–1838 (1999).
36. Wanunu, M., Sutin, J., McNally, B., Chow, A. & Meller, A. DNA translocation governed by interactions with solid-state nanopores. *Biophys. J.* **95**, 4716–4725 (2008).
37. Storm, A. J. *et al.* Fast DNA translocation through a solid-state nanopore. *Nano Lett.* **5**, 1193–1197 (2005).
38. Deamer, D. W. & Branton, D. Characterization of nucleic acids by nanopore analysis. *Acc. Chem. Res.* **35**, 817–825 (2002).
39. Kasianowicz, J. J., Brandin, E., Branton, D. & Deamer, D. W. Characterization of individual polynucleotide molecules using a membrane channel. *Proc. Natl Acad. Sci. USA* **93**, 13770–13773 (1996).
40. Maglia, G., Restrepo, M. R., Mikhailova, E. & Bayley, H. Enhanced translocation of single DNA molecules through alpha-hemolysin nanopores by manipulation of internal charge. *Proc. Natl Acad. Sci. USA* **105**, 19720–19725 (2008).
41. McNally, B., Wanunu, M. & Meller, A. Electromechanical unzipping of individual DNA molecules using synthetic sub-2 nm pores. *Nano Lett.* **8**, 3418–3422 (2008).
42. Skinner, G. M., van den Hout, M., Broekmans, O., Dekker, C. & Dekker, N. H. Distinguishing single- and double-stranded nucleic acid molecules using solid-state nanopores. *Nano Lett.* **9**, 2953–2960 (2009).
43. Meller, A. Dynamics of polynucleotide transport through nanometre-scale pores. *J. Phys. Condens. Matter* **15**, R581–R607 (2003).
44. Meller, A., Nivon, L., Brandin, E., Golovchenko, J. & Branton, D. Rapid nanopore discrimination between single polynucleotide molecules. *Proc. Natl Acad. Sci. USA* **97**, 1079–1084 (2000).
45. Smith, D. E., Perkins, T. T. & Chu, S. Dynamical scaling of DNA diffusion coefficients. *Macromolecules* **29**, 1372–1373 (1996).
46. Lam, P. M., Liu, F. & Ou-Yang, Z. C. Driven translocation of a polynucleotide chain through a nanopore: A continuous time Monte Carlo study. *Phys. Rev. E* **74**, 011911 (2006).
47. Lua, R. C. & Grosberg, A. Y. First passage times and asymmetry of DNA translocation. *Phys. Rev. E* **72**, 061918 (2005).
48. Mathe, J., Aksimentiev, A., Nelson, D. R., Schulten, K. & Meller, A. Orientation discrimination of single-stranded DNA inside the alpha-hemolysin membrane channel. *Proc. Natl Acad. Sci. USA* **102**, 12377–12382 (2005).
49. Peng, H. B. & Ling, X. S. Reverse DNA translocation through a solid-state nanopore by magnetic tweezers. *Nanotechnology* **20**, 185101 (2009).

Acknowledgements

This work is supported by the Air Force Office of Scientific Research grant FA 9550-10-1-0054, DOE Basic Energy Sciences grant DE-FG02-02-ER15368, US Department of Energy, Office of Basic Energy Sciences, Division of Materials Sciences and Engineering, and Sandia National Laboratories' LDRD program. Z.C. acknowledges DOE Basic Energy Sciences grant DE-FG02-02-ER15368 for carrying out nanopore-array fabrication and DNA translocation. D.R.D. acknowledges support from DOE Basic Energy Science grant DE-FG02-02-ER15368 and the Air Force Office of Scientific Research grant FA 9550-10-1-0054 for carrying out GISAXS and electrochemical deposition experiments. C.J.B. acknowledges the US Department of Energy, Office of Basic Energy Sciences, Division of Materials Sciences and Engineering and Sandia National Laboratories' LDRD program for conceiving the experiments and writing the paper. Y.J. acknowledges Sandia National Laboratories' LDRD program for carrying out ALD experiments. GISAXS experiments in this paper were conducted at the Advanced Photon Source at Argonne National Laboratory. Use of this facility is supported by the US Department of Energy, Office of Science, Office of Basic Energy Sciences, under contract DE-AC02-06CH11357. Sandia National Laboratories is a multiprogramme laboratory operated by Sandia Corporation, a wholly owned subsidiary of Lockheed Martin company, for the US Department of Energy's National Nuclear Security Administration under contract DE-AC04-94AL85000.

Author contributions

Z.C., C.J.B. and D.R.D. wrote the paper. C.J.B. conceived and directed the research. Z.C. carried out nanopore-array fabrication, DNA translocation and Fourier-transform infrared and N₂ adsorption experiments. Z.C. and Y.J. carried out TEM characterization and ALD experiments. D.R.D., H.W.H. and S.J.G. carried out GISAXS experiments. D.P.A. and C.H. carried out FIB lithography experiments. N.L. contributed to the DNA translocation set-up. D.R.D. carried out electrochemical-deposition experiments. N.R.A. and X.J. developed the transport model and carried out the simulations. Z.C. and N.Z. carried out PCR experiments.

Additional information

The authors declare no competing financial interests. Supplementary information accompanies this paper on www.nature.com/naturematerials. Reprints and permissions information is available online at <http://npg.nature.com/reprintsandpermissions>. Correspondence and requests for materials should be addressed to C.J.B.